The effect of braid angle on the flexural performance of structural braided thermoplastic composite beams

Anubhav Singh[a,*], Neil Reynolds[a], Elspeth M Keating[a], Alastair E Barnett[b], Steve K Barbour[b], Darren J Hughes[a]

[a] WMG, University of Warwick, Coventry CV4 7AL, United Kingdom
[b] Composite Braiding Limited, Derby DE24 9FU, United Kingdom

*Corresponding author, E-mail: A.Singh.10@warwick.ac.uk

https://doi.org/10.1016/j.compstruct.2020.113314

Abstract

Thermoplastic braided composite tubular beams were manufactured using commingled hybrid yarn with braid angles 30°, 45° and 60° and tested in static three-point flexure. Two principal deformation modes were observed during the flexural loading: global flexure and localised crush. The extent of each mode occurring in the three braid angle variants was measured using a linear deflectometer as well as 3D digital image correlation. Localised crushing was found to decrease significantly with increasing braided angle, accounting for 63%, 45% and 19% of the total applied deflection for the 30°, 45° and 60° beams respectively. Further, surface strain measurements obtained from 3D DIC showed increasing the braid angle led to a global flexure-dominated deformation. In addition, the stiffness and peak load increased with increasing braid angle. The observed differences in deformation modes were due to a combination of multiple braid angle-dependent properties of braided composites such as modulus, thickness etc.

Keywords: Braiding; Thermoplastic; Flexure; Localised crush; Digital image correlation

Introduction

The past three decades have seen braiding rise as a strong candidate among fibre reinforced polymer composite (henceforth referred to as composite) manufacturing techniques. Braiding involves the production of hollow tubular preforms by interlacing reinforcing fibres at an angle with respect to the axis of the preform. This is achieved by using a braiding machine, which enables bobbins loaded with the fibres to be moved in serpentine circular paths while pulling the free end of the fibres at a controlled velocity. During the braiding process, the shape and orientation of the braiding mandrel can be controlled, thus producing near-net shape preforms and minimising the wastes incurred due to trimming operations [1]. From a performance perspective, braided composite structures are known for their greater impact resistance compared to laminated composites with unidirectional fibres in each layer [2,3]. Owing to these advantages, braided composites find a wide range of applications in the automotive and aerospace industry [4].

The angle at which the fibres are interlaced with respect to the local axis of a braid is termed as braid angle. It is related with the braiding machine parameters as per Equation 1.

$$\alpha = \tan^{-1}\left(\frac{\omega_h D}{N_h v}\right) \quad (1)$$

where α: braid angle, ω_h: horn gear angular velocity (rpm), D: mandrel diameter (mm), N_h: number of horn gears and v: mandrel pull-off velocity (m/s).

Previous work has shown that the braid angle is directly related to the properties of the produced composite. For example, braiding at a higher braid angle leads to an increase in the thickness of the braided tows, therefore increasing the thickness of the braided component [5]. The mechanical properties of braided composites including elastic properties as well as mechanical strength have been shown to depend on braid angle [6–8]. Moreover, the braid angle has been reported to influence the deformation modes in braided composites. Under uniaxial tension, tubular braided specimens with small braid angles (<30°) were observed to show a linear elastic response until failure by Harte et al. [6], while specimens with large braid angles (>50°) showed a non-linear response accompanied with progressive necking, which delayed the ultimate failure. Similarly, Priem et al. [9] reported the failure mode of braided tubes under uniaxial compression to diverge from a splayed failure to a more stable progressive failure with an increase in braid angle.

The flexural response of braided composites has also been shown to depend on braid angle. For instance, Sturm et al. [10] conducted four-point bending tests of 38 mm wide and 400 mm long open section braided beams to assess their energy absorption characteristics for potential fuselage frame applications. It was observed that increasing the braid angle reduced the proclivity to flange buckling, hence improving energy absorption. As demonstrated by Sturm et al. [10], flexure tests performed using component scale specimens with complex geometries provide a direct assessment of structural performance. Unlike coupon level tests aimed at analysis and comparison of material properties, the response is a combination of specimens' material characteristics as well as geometry. Among the conventional flexural tests, three-point flexure is considered to be more relevant for structural applications as it is comparable to real-life load cases such as side impact on an automotive structure [11]. Therefore, three-point flexure has been used in several studies to evaluate the performance of side impact beams [12–14]. Moreover, three-point flexure allows for a combined assessment of resistance to localised crushing failure as well as global flexural deformation [11]. The localised crush in the impacted region manifests in different forms depending on the material and geometry of the specimens [15–20].

As mechanical behaviour of material as well as geometry are both directly related with braid angle, it is intuitive to expect braid angle to show a significant effect on localised crushing however, such a correlation has not been reported in the past. Previously reported studies on three-point flexure test response of braided rectangular coupons showed a decrease in flexural modulus and strength with increasing braid angle [21–23]. Moreover, increasing the braid angle was observed to delay the failure. Potluri et al. [24] conducted three-point flexure tests of tubular braided composites and reported similar trends of flexural modulus and strength as the results corresponding to rectangular coupons. These coupon-level studies showed a strong correlation between the flexural performance and braid angle. However, due to the coupons' geometry and scale, no localised deformations were reported. In contrast, the investigation conducted by Wu et al. [25] showed severe localised crushing during three-point flexure tests. However, the size of the loading roller and span to diameter ratio of the tested specimens were both inclined to induce localised crush over global flexure irrespective of braid angle. Moreover, the fibre volume fractions of the specimens were below 30%, which is not typical of structural composites. Thus, current literature lacks studies on three-point flexural response of braided structural composites, in particular investigating potential correlations between braid angle and multiple deformation modes, which dictate structural performance. Furthermore, existing literature focuses mainly on thermoset matrices, with no studies on thermoplastic matrix tubular braided materials.

This paper addresses this need through a systematic experimental study on component scale tubular braided beams. The results improve the current understanding of braided composite properties and their implications from a structural viewpoint. The presented work reports the flexural properties of tubular braided composite structures with a thermoplastic matrix for the first time.

Experimental methodology

Materials and manufacturing

A commingled E-glass/polyamide 6 (PA6) yarn from Coats [26] was used for braiding. The material characteristics of the commingled tows are listed in Table 1.

A 64-carrier braiding machine at Composite Braiding Limited was used to braid the commingled tows. Figure 1(a) shows the braiding process. The machine was used at half-capacity, i.e. 32 carriers, to produce a 1×1 diamond braid. Three braid angles were considered: 30°, 45° and 60°. For each braid angle, three layers of the commingled fabric were braided over 25 mm diameter mandrels to produce multi-layer braided preforms. Figure 1(b) shows flattened pieces cut from the braided preforms with different braid angles.

A bladder moulding process previously developed by the authors, called rapid variothermal moulding (RVM) [27], was used to produce tubular beams from braided commingled preforms. Figure 2(a) shows the steel tool used to mould the braided beams. The tool has a 530 mm long circular cavity with a diameter of 35 mm. The braided preforms were cut to the required length and then carefully removed from the mandrel. Prior to the moulding process, the braided preforms were dried in an industrial dryer at 70 °C for 24 hours to remove absorbed moisture from the fabric. A 1% drop in preform weight was observed after the drying process. A silicone rubber bladder was inserted through the preform and metallic end fittings were fit at both ends as shown in Figure 2(b).

During the RVM process, the tool was preheated to 150 °C and the preform-bladder assembly was placed into the mould cavity (tool). After closing the press, an internal bladder pressure of 4 bar was applied as the tool was heated to a consolidation temperature of 240 °C. This ensured that the braided fabric was in contact with the tool surface. On reaching the consolidation temperature, the pressure was increased to 20 bar. The temperature and pressure were maintained for 15 minutes, following which the tool was cooled to the demoulding temperature. The consolidation pressure and temperature were limited to 20 bar and 240 °C respectively because of the high temperature durability of the silicone rubber bladders. In order to minimise thermal distortion, the demoulding was carried out at a temperature of 50 °C, which is below the glass transition temperature of PA6. The bladder pressure of 20 bar was maintained during the cool-down phase. Figure 3 shows the temporal characteristics of the temperature and bladder pressure during RVM.

The outer and inner surfaces of the consolidated 30°, 45° and 60° braided beams produced using the RVM process are shown in Figures 4 (a), (b) and (c). The beams had smooth outer surfaces (due to contact with the tool), while the inner surfaces had the undulating texture of the braided fabric (due to contact with the flexible silicone rubber bladder). Similar to the flattened braids shown in Figure 1(b), an increase in the surface area covered by the fibres was observed with increasing braid angle. This was in agreement with previous studies [4]. Brownish discolouration was observed on the surfaces of the beams. On the outer surface, the degree of discolouration appeared to decrease with increasing braid angle, however, all the beams showed similar levels of

discolouration on the inner surfaces. Previous literature has linked this discolouration with thermo-oxidative chemical reactions of the PA6 [28,29]. A test was conducted where 5 cm long commingled tows extracted from the braided fabric were heated in ambient atmosphere and argon separately. The fabric retrieved after the thermal experiments are shown in Figures 4 (d) and (e). The fabric heated in the presence of argon displayed no discolouration, which confirmed that the interaction of ambient air with the PA6 at high temperature was responsible for the discolouration. Patches of dry fibres and intermittent fibre waviness were also observed on the outer surfaces of the consolidated beams.

A total of seven beams were manufactured for the braid angles of 30°, 45° and 60° and cut to a length of 420 mm. For six of the braided beams of each type, the braid angle was measured at 20 random locations on the outer surface and averaged. The measured braid angle values are shown for all the beams in Figure 5.

Part quality evaluation

In order to enable a comparison of the quality of consolidation in the braided beams, destructive (sectioning) evaluation was performed on one beam of each braid angle. The microstructure was analysed using optical microscopy to compare the defects between different beams. Moreover, the fractional composition of the beams was determined using resin burn-off tests.

The cross-section perpendicular to the beams' axes was selected for microstructural analysis. Approximately 10 mm-long cylindrical specimens were extracted by slicing the beams at two different locations using an abrasive wheel cutter. After slicing, the specimens were cold mounted in epoxy resin. The samples were polished using a Buehler EcoMet™ 300 automatic grinder-polisher to a 3 µm finish. Following the polishing operation, the samples were imaged using an automated stage ZEISS Axio Imager 2 microscope fitted with a 5 megapixel Axiocam 305 digital camera. A magnification of 5x was used. ZEISS ZEN 2 Core imaging software was used to perform stitching and generate images covering a wide area of the sample cross-section. Thickness variations within the braided beams were also measured from the polished samples using a macro zoom camera. The thickness was measured at a minimum of 350 locations taken from the two polished samples prepared for each braid angle. This was essential for capturing the non-uniform thickness distribution in the beams resulting from the undulating inner surfaces.

The resin burn-off experiments were conducted using the method introduced by Gupta et al. [30]. Six 20 mm long semi-circular specimens were cut from the braided beams, each weighing >500 mg. The density of each specimen was determined using the Archimedes principle as per BS EN ISO 1183-1 [31]. The thermal degradation of the resin was performed by heating the specimens to 500 °C using an 1800 Watt Milestone ETHOS UP High Performance Microwave heating system with ceramic furnace accessory. The fibre volume fractions (F_{vf}) and void volume fractions (V_{vf}) were subsequently determined as per BS EN ISO 14127 [32].

Quasi-static three-point flexure tests

An Instron 5800R test machine equipped with a 100 kN load cell was used to perform quasi-static three-point flexure experiments. The test setup is shown in Figure 6(a). Test control and data collection were performed using the Instron material testing software Bluehill version 2. During the test, the beams were supported over a test span of 350 mm on rollers having a diameter of 40 mm. A central loading roller of 100 mm diameter was used. The effect of through-thickness beam shear during the flexural deformation was analytically determined

using the approach presented by Tolf et al. [33]. The induced deviation from pure flexure is less than 10% for the span-to-depth ratio corresponding to the beams and test geometry used in this study.

In order to measure the flexural displacement at the bottom surface of the beams, an Instron 2630-112 extensometer was used in deflectometer mode. The extensometer was attached to a spring-loaded plunger, thus making a linear deflectometer, as shown in Figure 6(b). The deflectometer assembly was rigidly fixed onto the test bed such that the tip of the plunger maintained contact with the lower surface of the beam throughout the flexural deformation. The difference between the measured bottom surface displacement and the applied crosshead displacement was used to evaluate the localised crushing propagating from the top surface. Six repeats of each braid angle were tested in three-point flexure, out of which the bottom surface displacement was recorded for 3 repeats.

Before each test, the beam was preloaded to 10 N to ensure full engagement of the upper loading roller with each beam before starting the test. The test was carried out at a constant crosshead displacement rate of 10 mm/min, which corresponds to a flexural strain rate of less than 2 %/min. The test data (load, crosshead position and deflection) was recorded at a rate of 10 Hz. Dedicated experiments were performed to evaluate the compliance of the test setup and the precision of the load cell in the load range observed during the flexural testing of the braided beams. Results of these experiments indicated that a maximum displacement of 0.03 mm was induced due to the setup compliance at maximum load, while the maximum error in the load cell measurements was less than 2%.

Digital image correlation

In order to measure and compare the surface strains during three-point flexure, a three-dimensional digital image correlation (DIC) system was used during the flexure test for one repeat of each braid angle. As demonstrated in literature [34,35], DIC is useful for recording the multiaxial strains as well as out-of-plane deformations induced during flexural testing.

The DIC measurements in this work were performed on images obtained using a matched pair of GOM 12M digital cameras. The lenses attached to the cameras had a focal length of 100 mm. Commercially available DIC software GOM ARAMIS [36] version 6.1 was used to acquire and analyse the DIC images. As the majority of deformation was observed to occur in the contact region directly under the loading roller, the central segment of the beams was selected as the Region of Interest (RoI). It should be noted that the surface strain measurements were made on the region of the beam surface visible to the cameras. The area undergoing the damage was beneath the central loading roller and therefore could not be captured within the view of the cameras. After mounting the measurement system, both the cameras were focused on a plane tangential to the circular surface of the braided beam closest to the cameras. Twin-LED lights were used to illuminate the RoI during the experiments. A schematic of the three-point flexure setup with the DIC measurement system is shown in Figure 7. The DIC system and software parameters are listed in Table 2.

In order to ensure consistency, DIC calibration and the flexure experiments were performed under precisely the same conditions. Prior to performing three-dimensional calibration of the optical apparatus, the cameras were turned on and allowed to warm up and equilibrate with the entire system for 30 minutes. The obtained calibration deviation was within the GOM ARAMIS recommended threshold of 0.04 pixels, indicating a

successful calibration. The RoI of every beam was prepared for the optical strain measurement by applying a stochastic white speckle pattern on a matt black background. Firstly, the beam surfaces were coated with a black coloured base using a Plastikote Black Primer. The black base was allowed to dry fully, following which the white speckle pattern was sprayed onto the RoI using a Badger air brush using generic white emulsion paint diluted to approximately 50% by volume.

The post-processing of the DIC data was conducted using GOM Correlate Professional software [37]. For every beam, the software creates a surface component using the recognised facets. In order to ensure that the measured displacements are aligned correctly with respect to the tested beam, a modified alignment was created using an imported CAD geometry. For every beam, six static images were captured after preloading the beam. These images were analysed to estimate the measurement accuracy as well as evaluate the fitness of the pattern and the calibration for successful acquisition of DIC data. Figure 8 shows the strain distribution in a static image in the preload condition. The 'false' strain values shown in the figure arise due to sensor noise. The 'false' strain is randomly distributed across the entire image without any localised anomalies, as shown in the figure, indicating that the measurement system is correctly set up. Assuming that the strain measurements in static images are normally distributed, the mean of these falsely determined strains and displacements represent the bias of the measurement, while the standard deviations represent the resolution of the measuring system [38]. These statistical metrics for DIC data are listed in Table 3.

Results and discussion

Evaluation of part quality

The F_{vf} and V_{vf} values of the braided beams determined from resin burn-off experiments are listed in Table 4. Single-factor analysis of variance (ANOVA) was performed to statistically compare the F_{vf} and V_{vf} obtained for the three braid angles. A 95% confidence level was used. The corresponding p-values for both the F_{vf} and V_{vf} comparisons are listed in Table 5. The p-value corresponding to F_{vf} is greater than 0.05. Therefore, the ANOVA results indicate that the F_{vf} values did not differ significantly between the braided beams with different braid angles. The lack of correlation between F_{vf} and braid angle was due to the predetermined composition of the commingled preforms used to manufacture the braided beams. Similar observation was reported by Laberge-Lebel [23] for rectangular braided coupons manufactured using a commingled carbon fibre-PA12 system. However, the p-value for V_{vf} is less than 0.05, which indicates that the void content was significantly different between the three beams. In order to analyse the difference in the V_{vf} values, a post hoc analysis was performed using the Tukey-Kramer method [39]. As per the method, the Studentised range statistic q was evaluated for each pair using Equation 2.

$$q_{AB} = \frac{|\mu_A - \mu_B|}{\sqrt{\frac{MS_W}{2}\left(\frac{1}{n_A}+\frac{1}{n_B}\right)}} \quad (2)$$

where q_{AB}: q-statistic for the pair A-B; μ_A: mean for sample A; μ_B: mean for sample B; n_A: sample size of A; n_B: sample size of B and MS_W: mean square error within samples.

If the evaluated q value is greater than the critical value of q, determined from the q-table, it implies that the difference between the means corresponding to the respective pair of samples is statistically significant. The obtained q-values corresponding to every comparison are listed in Table 6.

The results indicate that the V_{vf} of the 30° and 45° beams are similar, while the voidage is greater for the 60° beams. As higher void content typically results in reduced mechanical properties of composite structures [40], the three-point flexural response of the 60° beams would be expected to be more severely affected as compared to the 30° and 45° beams.

The measured thickness values were distributed in increasing bands of 0.05 mm between the maximum and minimum values for each braid angle. The resulting distributions are shown in Figure 9 in the form of frequency line plots. The mean, maximum and minimum thickness for each braid angle are listed in Table 7. The histograms show that the thickness increases with braid angle. The mean thickness increased by 18% from the 30° to 45° beam, while the increase from 45° to 60° was 42%.

Braided tow width was measured on the outer surface of the untested braided beam for each braid angle at 25 randomly located points. The measured tow width was used to determine analytically the cover factor, i.e. surface area of the braided composite covered by the braided fibres, as per Equation 3. Further details of the analytical calculations can be found in references [41,42].

$$\text{Cover factor} = 1 - \left(1 - \frac{wN_c}{2\pi D \cos\alpha}\right)^2 \quad (3)$$

where w: tow width (mm) and N_c: number of carriers used in braiding.

Table 8 shows the measured tow width and the analytically estimated cover factor for beams with different braid angles. The width of the tows decreased with increasing braid angle, while the cover factor increased, which is in agreement with previously reported results.

Figure 10 shows selected micrographs of the three beams (30°, 45° and 60°). The observed material distribution displaying resin rich pockets between fibre tows is characteristic to braided composites. Three types of voids were identified from the micrographs:

(a) Intra-tow micro voids: Circular voids visible as dark spots between fibre filaments.

(b) Intra-tow macro voids: An agglomeration of multiple micro-voids that lead to the formation of larger voids, often elliptical in shape.

(c) Inter-tow voids: Voids in the resin-rich pockets between fibre-tows.

In addition to void fraction, void characteristics such as location, morphology and distribution also individually influence mechanical performance [43,44]. Therefore, particle analysis was performed using the image processing software ImageJ (release 1.49v) [45] to quantify and compare the size and shape of the voids observed in the micrographs. Figure 11 shows histograms representing the size distribution of voids for 30°, 45° and 60° beams.

The shape of the voids was quantified using the circularity parameter C in ImageJ, shown in Equation 4.

$$C = \frac{4\pi A}{P^2} \quad (4)$$

where A: area (μm^2) and P: perimeter (μm).

A circularity value of 1 represents a perfect circle, whilst a value approaching 0 corresponds to a stretched elliptical shape. Figure 12 shows histograms representing the shape distribution of voids for the 30°, 45° and 60° beams.

The size and shape distributions for different braid angles were assessed through ANOVA. The obtained p-values are listed in Table 9. As both p-values are less than 0.05, it was concluded that the difference between the size and shape distributions of the voids is statistically significant between the braided beams with different braid angles. Results of the Tukey-Kramer post-hoc analysis, shown in Table 10, revealed that voids in 60° beam were larger, while those in 30° and 45° beams did not differ significantly. On the other hand, the circularity of the voids was the greatest in the 45° beams followed by 60° and 30° in that order. Previously conducted investigations have shown that effects of the void characteristics on mechanical performance are specific to material as well as load cases [46]; it is therefore proposed that a discrete work package would be required to establish the absolute effect of voidage on the performance of the beams tested in this work, which was considered out of scope of this study.

Static three-point flexure performance

Figure 13 shows the load-crosshead displacement curves obtained from the three-point flexure tests. The crosshead displacement was limited to 18 mm for all the beams, as further applied displacements led to visible lateral movement at the beam-support roller interface.

The load-displacement curves corresponding to different braid angles form three discrete populations. This indicates a significant dependence of the mechanical response on braid angle, which directly influences both material properties and beam thickness. Each response showed an initial increase in load. During this load rise, audible cracking was noted for all the beams. For the 60° beams, the load generally increased throughout the deformation, with a visible plateauing within the last one millimetre of crosshead displacement. On the other hand, for the 45° and 30° beams, the load increased to a local maximum followed by undulating load profiles with multiple peaks and troughs, ending with an ultimate steady decline.

Figure 14 shows one deformed beam for each braid angle in the test setup before unloading. The visible differences in the cross-sectional depth and bottom surface curvatures between the three beams indicate the correlation between the deformation modes and braid angle. Cracks were observed ex-situ in the loading area for every beam. These cracks originated in the region in direct contact with the loading roller and propagated along the braided fibres. None of the beams had visible damage in the region of the beam opposite the central loading point. A closer view of the unloaded deformed beams revealed that there was a transition from a single-region contact at the start of the test to a double-region contact at the loading roller-beam interface. The contact transitions were more noticeable for the 30° and 45° beams as compared to the 60° beams. Therefore, it is reasonable to assume that the localised contact-dependent damage propagation was responsible for the variable trends observed in the load-displacement curves. After unloading the beams, the 30° and 45° beams returned to their original shape, while the 60° beams had a noticeable permanent curvature.

The extent of localised crushing, recorded using the deflectometer assembly, is plotted against crosshead displacement in Figure 15. The curves show that the localised crushing initiated with the onset of flexural deflection and progressed with an approximately linear trend. For a crosshead displacement of 18 mm, the

localised crushing accounted for approximately 63%, 45% and 19% of the applied crosshead deflection for 30°, 45° and 60° beams respectively. Therefore, localised crush was the dominant deformation mode for the 30° beams, while global flexure was observed to dominate for the 60° beams. The response of the 45° beams was intermediate between the 30° and 60° beams.

The stiffness of the braided beams during the three-point flexure tests was determined using a chord definition represented in Equation 5.

$$S = \frac{\Delta P}{\Delta d} \quad (5)$$

where S: stiffness (N/mm); P: load (N) and d: displacement (mm).

The displacement range between 0.2 mm and 1 mm was considered for the stiffness calculations. In this range, the per cent localised crushing was 62%, 38% and 15% for the 30°, 45° and 60° beams respectively. The 60° beams showed the highest stiffness and peak load values, which are shown for the three braid angles in Figure 16. It is important to note that stiffness and peak load here are indicators of structural mechanical response, which is a combination of the beams' material characteristics as well as the beam sections' geometric properties. The average stiffness of the 45° and 30° beams were 14% and 36% lower relative to the 60° beams respectively. Similarly, the average peak load values were 37% and 57% lower respectively. This suggests that the effect of the aforementioned observed small disparity in void content is not a dominant factor upon the flexural response and the analysis based on the braid angle of beams remains meaningful. A dedicated experimental program is required to establish the actual effect of void size and shape distributions.

The observed trends of stiffness and peak load are in disagreement with the results reported by Potluri et al. [24] using coupon scale beams. This disagreement was likely due to the localised crushing observed in the present study which was not observed previously. However, the work by Potluri studied thermoset matrix-based composites and did not report the number of test repeats, which made it difficult to perform a conclusive comparison.

DIC analysis

The evolution of x-strain (ε_x), i.e. surface strain along the beam axis, is shown for the three braid angles in Figure 17(a). The load-crosshead displacement response of the beams tested with the DIC measurements are also shown in Figure 17(b) for reference. A non-uniform distribution was observed in all the strain profiles. The strain profile corresponding to the 60° beam approximates to pure flexure with distinguishable bands of compressive and tensile strains of similar magnitude in the top and bottom regions of the beam. These strain bands were symmetric about the central load introduction point and maintained their trends with increasing deflection. The effect of localised crushing appeared towards the end of the deformation in the form of minimal observable strain localisation in the upper loading region. Contrary to the 60° beam, the severe localised crushing in the 30° beam resulted in concentrated zones of compressive strain in the top region (around the central roller), while negligible strain was observed in the bottom region. With increasing crosshead displacement, the cracks propagated from the central loading point and appeared in the RoI. This was accompanied by further strain concentration in this loading region. The 45° beam showed emerging compressive and tensile strain bands similar to the 60° beam during the initial phase. However, the magnitude of the bottom region tensile strain was significantly lower. As the localised damage progressed into the RoI, strains became concentrated in the upper loading region similar to the 30° beam.

In order to further explore the differences in strain distribution that arose during loading of the beams, three parallel horizontal sections were constructed on the beam surface using the GOM software, as shown in Figure 18(a). The figure also shows that the three computed sections flex with the increasing deformation. Along each section, the GOM Correlate interface was used to evaluate flexural strain, computed as the average of the axial strains calculated at all integration points along the chosen line section. The evolution of the flexural strains 1, 2 and 3, corresponding to the top, middle and bottom regions respectively, are plotted against crosshead displacement for different braid angles in Figures 18(b), (c) and (d). Irrespective of braid angle, the top and bottom region strains (strain 1 and 3) showed increasing compressive and tensile trends respectively throughout the deformation. Owing to the localised deformation, the top region strain measurements (strain 1) became invalid for the 30° and 45° beams once damage propagated into the uppermost section. Until that point, the top region strains showed comparable magnitudes for all braid angles. On the contrary, the strains in the bottom region (strain 3) calculated for the 30° and 45° beams were low in magnitude in comparison to the 60° beam. Quantitatively, the bottom region strains at test completion (a crosshead displacement of 18 mm) were 77% and 91% lower for 45° and 30° beams respectively as compared to the 60° beam. In the middle region (strain 2), the flexural strains were initially tensile for all the braid angles. However, as the deformation advanced and the 30° and 45° beams collapsed under the loading roller, the recorded strains transitioned into compressive domain, while the obtained strain in the corresponding middle region in the 60° beam remained tensile.

In addition to these flexural strain analyses, three parallel sections were constructed on the beam surface using the GOM software, as shown in Figure 19(a). The downward (y-) displacements were recorded on all the points lying on these sections with respect to the crosshead. Figure 19(b) shows the progression of section-wise y-displacements y1, y2 and y3 with increasing crosshead displacement. The increase in disparity between the three section-wise displacements with decreasing braid angle is a representation of the departure from pure global flexure and into localised crush. Moreover, the increasing curvature of y3 with increasing braid angle further indicates the escalation of tensile deformation in the bottom region. It should be noted that the size of the error metrics presented in Table 3 are very small as compared to the obtained means and observed differences in the optically-measured strains and displacements between the three types of braided beams.

The results are interesting in that the DIC measurements show that with decreasing braid angle, the bottom halves of the braided beams showed decreasing tendency away from flexural deformation. This was due to the localised crushing in the upper half of the beam accommodating most of the applied crosshead displacement. Moreover, the higher tensile strain measured in the bottom half of the 60° beam explains the plastic deformation (permanent curvature) observed after unloading.

The observed braid-angle dependence of the overall mechanical response is attributed to three braid angle dependent factors:

(i) Thickness: As per classical beam flexure theory, increasing the section thickness increases its section modulus, hence improving the structure's resistance to flexural deformation. Furthermore, a hollow section's proclivity for localised crushing decreases with increasing wall thickness. Therefore, an increase in wall thickness makes the beam more resistant against both deformation

modes and is expected to render an improvement in mechanical response. As observed in previous studies as well as discussed here, the thickness of braided beams increases with braid angle.

(ii) Material moduli: Theoretically, axial modulus of a material is positively correlated to the resistance to flexural deformation in a structure via an increase in section modulus. On the other hand, transverse modulus, directed along the hoop direction for a circular beam, would strengthen a beam structure against local crushing. For a braided composite, previously reported experimental data has clearly shown that axial modulus decreases with braid angle, while transverse modulus increases [6-8].

(iii) Surface Coverage: The resin rich pockets present on the surface - as well as in the internal structure - often act as damage initiation sites for braided composites [47,48]. As displayed through analytical estimates presented in Table 8, the surface fibre coverage of the braided beams increased with increasing braid angle. Therefore, the 30° beams, having the least fibre coverage, had relatively larger resin rich pockets on the outer surface, followed sequentially by the 45° and 60° beams. Therefore, it is proposed that the interaction of the central loading roller with the increased level of resin rich regions in the 30° beams contributes to early initiation and propagation of localised damage.

The flexure test results show that increasing the braid angle resulted in enhanced mechanical performance. Moreover, the poorer mechanical performance of the lower braid angles coincided with greater local crushing. Considering the observed trends of the three discussed braid-angle dependent features as well as their expected influence upon deformation behaviour, the flexure test results indicate that resistance to localised crush was the critical performance factor for the beams characterised in this study. It is proposed that localised crush is an important consideration for thermoplastic composites in this particular loading configuration because of the lower stiffness and higher ductility of the matrix compared to thermosetting matrices, and thus explains any disagreement of the results obtained in this study with previously reported results from studies on the latter material type.

Conclusions

The static three-point flexure response of component scale thermoplastic braided composite beams with braid angles of 30°, 45° and 60° was investigated. The flexural deformation manifested through two principal modes: localised crushing and global flexure. Localised crushing was observed to account for 63%, 45% and 19% of the total deflection for the 30°, 45° and 60° beams respectively at the point of maximum experimental deflection. Surface strain profiles obtained using three-dimensional DIC showed significant variation between the beams with different braid angles, particularly on the lower (tensile) face furthest away from the loading point. Analysis of the flexural strains as well as the transverse displacements showed significant tensile deformation in the bottom region for the 60° beam. On the other hand, the localised crush-dominant deformation led to minimal applied strains in bottom regions of the 30° and 45° beams. Consequently, the 30° and 45° beams returned to their original shape after unloading while the 60° beams underwent permanent (plastic) deformation due to the much higher applied strains. Increasing the braid angle resulted in improvement in mechanical performance,

with significant increases observed in stiffness as well as peak load. Three braid angle dependent factors: thickness, material moduli and surface fibre coverage, were identified as the contributing factors to the observed differences in the mechanical performance as well as deformation modes. Based on the trends and independent influence of these features on flexural performance, resistance to localised crushing proved to be the critical factor governing the mechanical response of the braided beams tested in this work. The observed trends of flexural performance disagreed with previously reported flexural results of coupon scale braided beams, which could be attributed to the effect of beams' scale and test geometry as well as the use of relatively ductile lower stiffness thermoplastic matrix as opposed to thermoset matrices as studied previously. As such, the reported results establish a clear correlation between braid angle and deformation modes during the three-point flexural testing of thermoplastic braided beam structures. Detailed analysis and comparison of voidage in the braided beams was conducted using microscopy and resin-burn off experiments. A statistically significant difference in void morphology according to braid angle was observed, but the analysis revealed that these differences in void content/morphology did not affect mechanical performance as strongly as braid angle, and as such effects were not able to be measured. Therefore, a controlled study is required to understand the effects of voids on three-point flexural performance in such braided thermoplastic composite beam structures. Finally, as the current study is limited to thermoplastic braided composites with a biaxial regular braid pattern, the authors consider that a study of trends in flexural performance obtained using thermoset-based braided composites as well as triaxial braid patterns would be useful additions to the body of work in this area.

Acknowledgements

The authors are thankful to the technical staff at WMG and Composite Braiding Limited for their time and support in this work.

Funding source

The author (Anubhav Singh) was funded through a WMG departmental scholarship.

Data Availability Statement

The raw/processed data required to reproduce these findings cannot be shared at this time as the data also forms part of an ongoing study.

References

[1] Kelkar AD, Whitcomb JD. Characterization and structural behavior of braided composites. U.S. Department of Transportation Federal Aviation Administration. 2009.
[2] Arold B, Gessler A, Metzner C, Birkefeld K. Braiding processes for composites manufacture. In: Advances in Composites Manufacturing and Process Design. Woodhead Publishing; 2015, p. 3-26.
[3] Verpoest I. Composite preforming techniques. In: Polymer matrix composites. Elsevier Science Limited; 2000, p.623-669.
[4] Carey JP. Introduction to braided composites. In: Handbook of Advances in Braided Composite Materials. Woodhead Publishing; 2017, p. 1–21.
[5] Gautam M, Potluri P, Ogin S, Jain P. Necking behaviour of flattened tubular braided composites. In: ICCM 2015: Proceedings of the 20th International Conference on Composite Materials, Copenhagen, July 2015.
[6] Harte AM, Fleck NA. On the mechanics of braided composites in tension. Eur J Mech A/Solids 2000;19:259–75.
[7] Melenka GW, Carey JP. Development of a generalized analytical model for tubular braided-architecture composites. J Compos Mater 2017;51:3861–75.

[8] Falzon PJ, Herszberg I. Mechanical performance of 2-D braided carbon/epoxy composites. Compos Sci Technol 1998;58:253–65.
[9] Priem C, Othman R, Rozycki P, Guillon D. Experimental investigation of the crash energy absorption of 2.5D-braided thermoplastic composite tubes. Compos Struct 2014;116:814–26.
[10] Sturm R, Heieck F. Energy absorption capacity of braided frames under bending loads. Compos Struct 2015;134:957–65.
[11] Reynolds N, Ramamohan AB. High-volume thermoplastic composite technology for automotive structures. In: Advanced composite materials for automotive application. Joh Wiley & Sons; 2013, p. 29–50.
[12] Cheon SS, Lee DG, Jeong KS. Composite side-door impact beams for passenger cars. Compos Struct 1997;38:229–39.
[13] Rebelo PM. Design Study of a Side Intrusion Beam for Automotive Safety. MSc Thesis, Instituto Superior Técnico, Lisboa, 2016.
[14] Calonghi A. Alternative design of front door side impact beam for Nissan Navara. MSc Thesis, Cranfield University, 2006.
[15] Belingardi G, Mehdipour H, Mangino E, Martorana B. Progressive damage analysis of a rate-dependent hybrid composite beam. Compos Struct 2016;154:433–42.
[16] Bilston D, Rathnaweera G, Ruan D, Hajj M, Durandet Y. Parametric study of the bending properties of lightweight tubular metal/polymer foam hybrid structures. Compos Part B Eng 2016;105:101–10.
[17] Gardner L, Nethercot DA. Experiments on stainless steel hollow sections—Part 2: Member behaviour of columns and beams. J Constr Steel Res 2004;60:1319–32.
[18] Tang T, Zhang W, Yin H, Wang H. Crushing analysis of thin-walled beams with various section geometries under lateral impact. Thin-Walled Struct 2016;102:43–57.
[19] Kecman D. Bending collapse of rectangular and square section tubes. Int J Mech Sci 1983;25:623–36.
[20] Liu Q, Xing H, Ju Y, Ou Z, Li Q. Quasi-static axial crushing and transverse bending of double hat shaped CFRP tubes. Compos Struct 2014;117:1–11.
[21] Fujihara K, Yoshida E, Nakai A, Ramakrishna S, Hamada H. Influence of micro-structures on bending properties of braided laminated composites. Compos Sci Technol 2007;67:2191–8.
[22] Tate JS, Kelkar AD. Flexural behavior of biaxial braided composites. In: Proceedings of ASME International Mechanical Engineering Congress and Exposition, Orlando, November 2005.
[23] Laberge-Lebel L, Van Hoa S. Manufacturing of braided thermoplastic composites with carbon/nylon commingled fibers. J Compos Mater 2007;41:1101–21.
[24] Potluri P, Manan A, Francke M, Day RJ. Flexural and torsional behaviour of biaxial and triaxial braided composite structures. Compos Struct 2006;75:377–86.
[25] Wu Z, Shen Y, Pan Z, Hu X. Three-point Bending Behavior and Energy Absorption Capacity of Composite Tube Reinforced by Gradient Braided Structure in Radial Direction. Fibers Polym 2019;20:1455–66.
[26] Coats. Coats Synergex.
Available from: https://www.coats.com/en/Guidance/CoatsSynergex#Commingling (accessed March 27, 2020).
[27] Singh A, Reynolds N, Carnegie CR, Micallef C, Keating EM, Winnett J, et al. A novel route for volume manufacturing of hollow braided composite beam structures. Adv Manuf Polym Compos Sci 2019:1–6.
[28] Grigg MN. Thermo-oxidative degradation of polyamide 6. PhD Thesis, Queensland University of Technology, 2006.
[29] Tung JF. Synthesis and characterisation of polyamide 6 blends made by reactive extrusion. PhD Thesis, Brunel University, 1993.
[30] Gupta J, Reynolds N, Chiciudean T, Kendall K. A comparative study between epoxy and vinyl ester CF-SMC for high volume automotive composite crash structures. Compos Struct 2020;244:112299.
[31] BS EN ISO 1183-1. Plastics. Methods for determining the density of non-cellular plastics—Part 1: Immersion method, liquid pycnometer method and titration method. BSI 2019.
[32] BS EN ISO 14127:2008. Carbon-fibre-reinforced composites. Determination of the resin, fibre and void contents. BSI 2008.
[33] Tolf G, Clarin P. Comparison between flexural and tensile modulus of fibre composites. Fibre Sci Technol 1984;21:319–26.
[34] Unlusoy C, Melenka GW. Flexural testing of cellulose fiber braided composites using three dimensional digital image correlation. Compos Struct 2019;230:111538.
[35] Makeev A, Ignatius C, He Y, Shonkwiler B. A Test Method for Assessment of Shear Properties of Thick Composites. J Compos Mater 2009;43:3091–105.
[36] GOM. GOM ARAMIS. Available from: https://www.gom.com/metrology-systems/aramis. (accessed March 27, 2020).
[37] GOM. GOM Correlate Professional. Available from: https://www.gom.com/3d-software/gom-correlate-professional.html. (accessed March 27, 2020).

[38] Powe RAW. Towards the characterisation of automotive specific woven composite laminates at intermediate strain rates. PhD Thesis, University of Warwick. 2018.
[39] Tukey JW. The collected works of John W. Tukey. vol. 1. Taylor & Francis; 1984.
[40] Olivier P, Cottu JP, Ferret B. Effects of cure cycle pressure and voids on some mechanical properties of carbon/epoxy laminates. Composites 1995;26:509–15.
[41] Potluri P, Manan A. Mechanics of non-orthogonally interlaced textile composites. Compos Part A Appl Sci Manuf 2007;38:1216–26.
[42] Melenka, G.W., Hunt, A.J., van Ravenhorst, J.H., Akkerman, R., Pastore, C.M., Ko, F.K., Munro, M., Carey, J.P. Manufacturing processes for braided composite materials. In: Handbook of Advances in Braided Composite Materials. Woodhead Publishing; 2017, p. 47–153.
[43] Lambert J, Chambers AR, Sinclair I, Spearing SM. 3D damage characterisation and the role of voids in the fatigue of wind turbine blade materials. Compos Sci Technol 2012;72:337–43.
[44] Patou J, Bonnaire R, De Luycker E, Bernhart G. Influence of consolidation process on voids and mechanical properties of powdered and commingled carbon/PPS laminates. Compos Part A Appl Sci Manuf 2019;117:260–75.
[45] Schneider CA, Rasband WS, Eliceiri KW. NIH Image to ImageJ: 25 years of image analysis. Natural Methods 2012;9:671–5.
[46] Mehdikhani M, Gorbatikh L, Verpoest I, Lomov S V. Voids in fiber-reinforced polymer composites: A review on their formation, characteristics, and effects on mechanical performance. J Compos Mater 2019;53:1579–669.
[47] Bibo GA, Hogg PJ. The role of reinforcement architecture on impact damage mechanisms and post-impact compression behaviour. J Mater Sci 1996;31:1115–37.
[48] Fouinneteau M. Damage and failure modelling of carbon and glass 2D braided composites. PhD Thesis, Cranfield University. 2006.

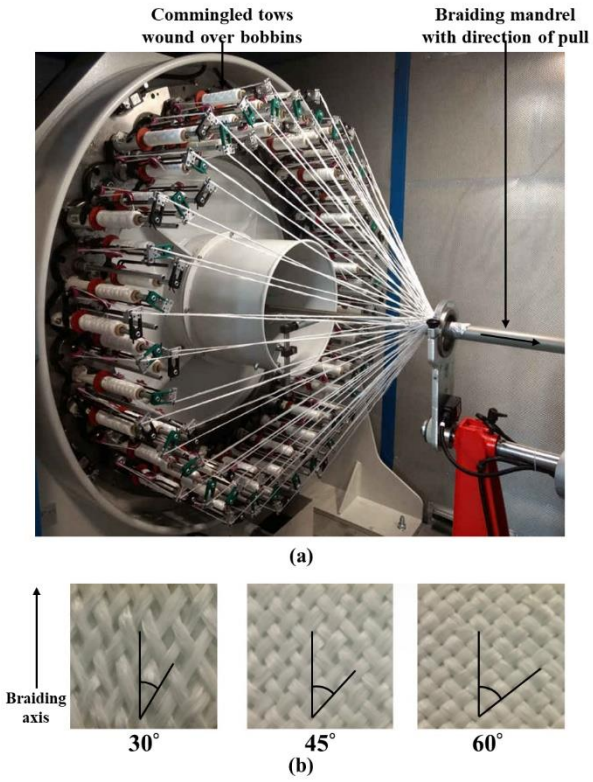

Figure 1 (a) Braiding of commingled tows and (b) flattened 1×1 diamond preforms with braid angle of 30°, 45° and 60°

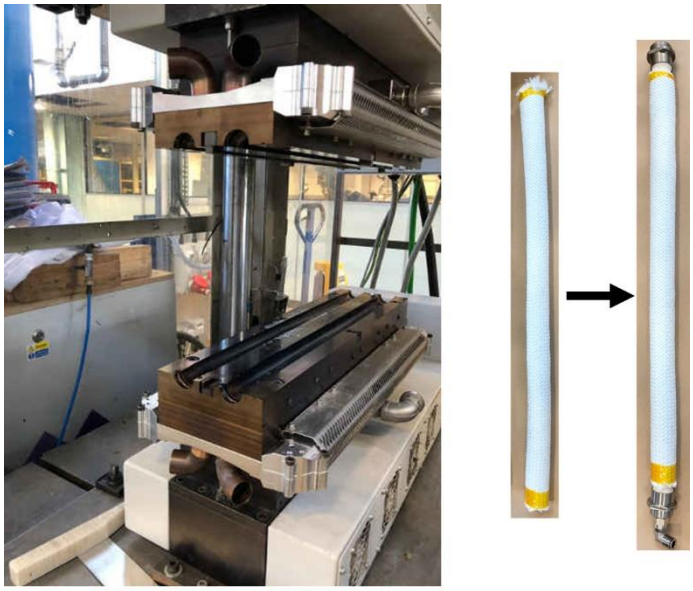

Figure 2 (a) RVM tool used for moulding of braided beams and (b) preparation of bladder-preform assembly from braided fabric

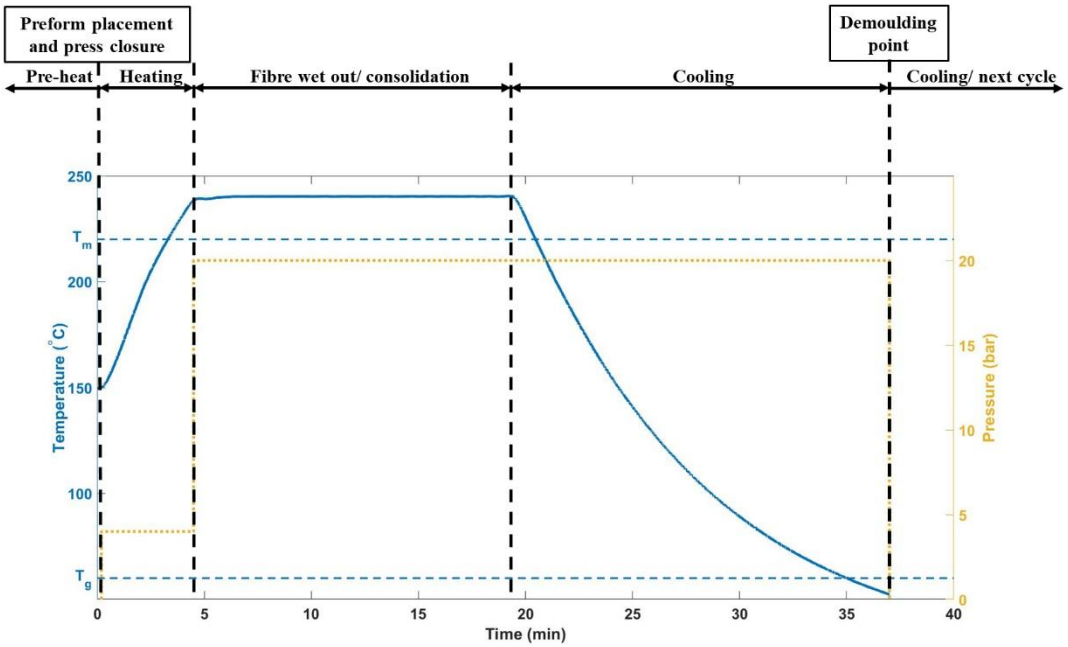

Figure 3 RVM process profile showing temporal characteristics of pressure and temperature during the process cycle. Note: melt temperature (T_m) and glass transition temperature (T_g) of PA6 are shown for reference

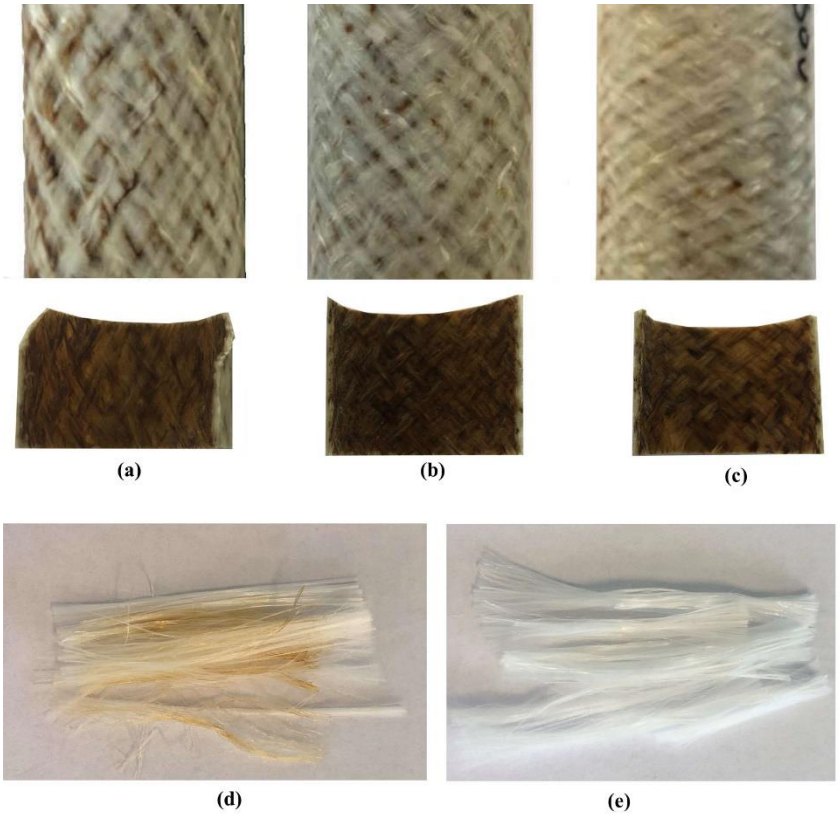

Figure 4 Outer and inner surfaces of (a) 30°; (b) 45° and (c) 60° braided beam; retrieved commingled fabric after heating to 250 °C: (d) visible brownish discolouration upon heating in ambient atmosphere with exposure to air and (e) no discolouration upon heating in an inert argon atmosphere

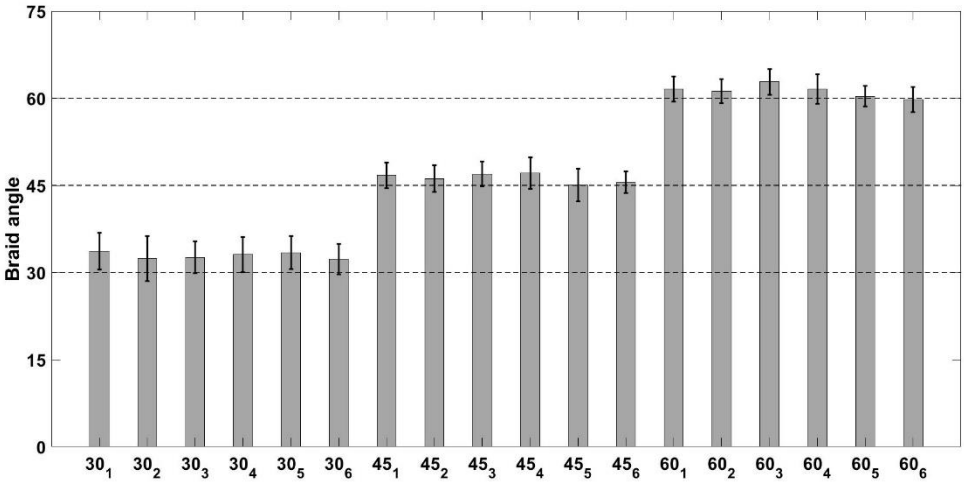

Figure 5 Measured braid angle for all the braided beams (30°, 45° and 60°). Note: values represent mean ± std. dev.

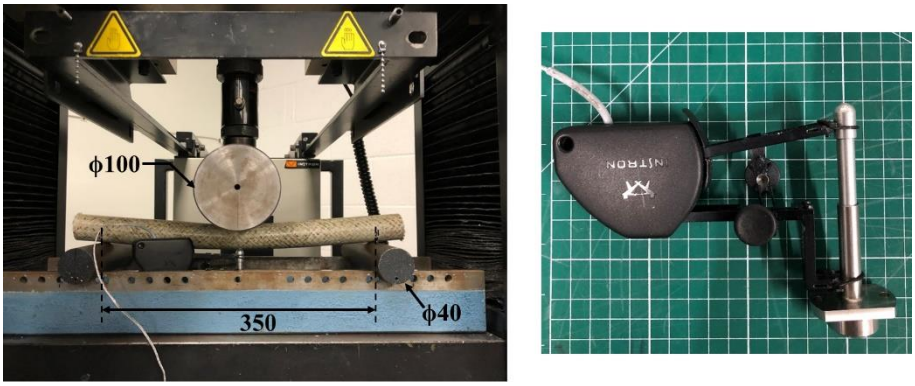

Figure 6 (a) Three-point flexure setup on the test machine frame and (b) deflectometer assembly. Note: all units are in mm

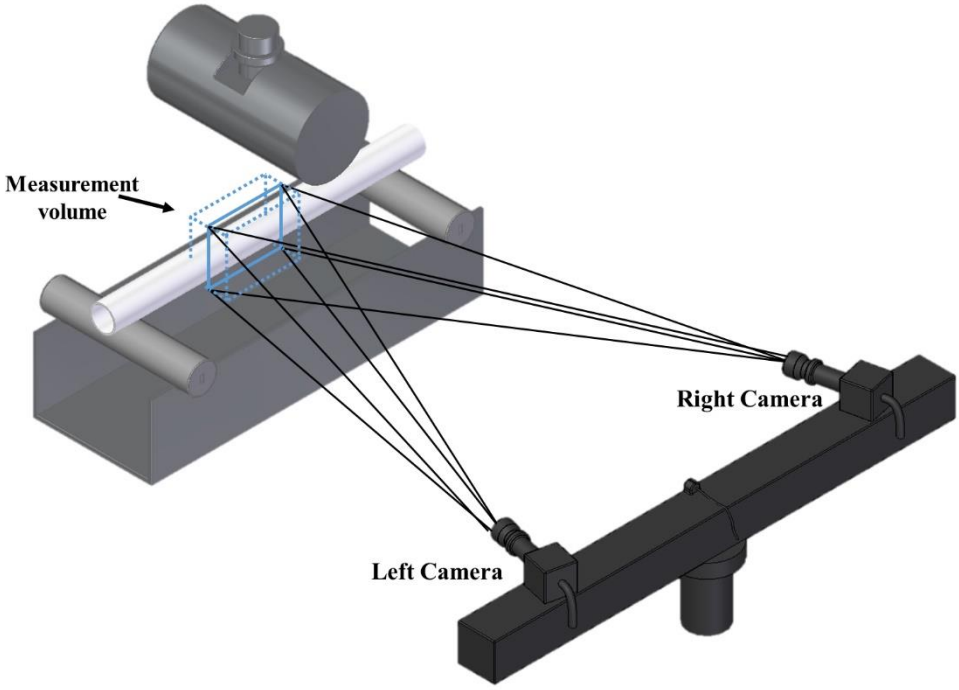

Figure 7 Schematic of DIC measurement during three-point flexure test

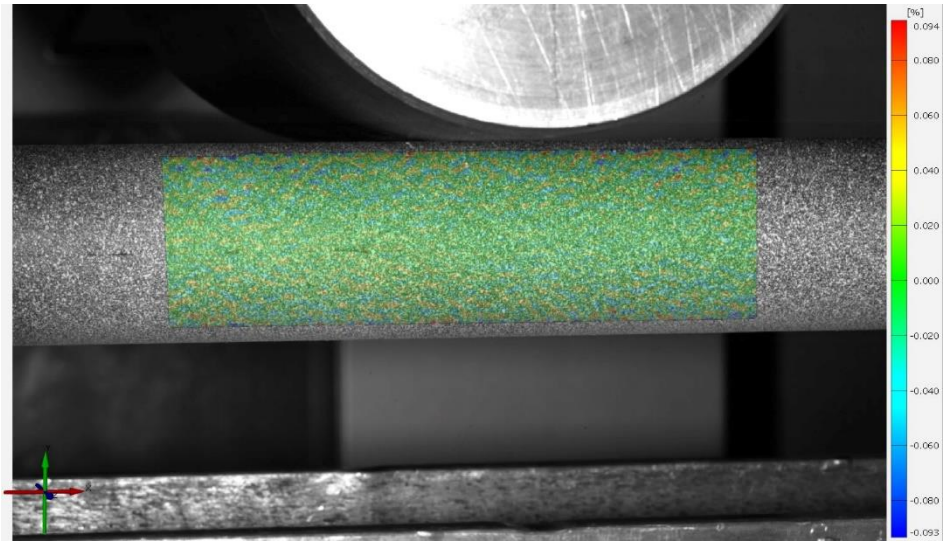

Figure 8 Static image in the preload condition with a distribution of false strain values

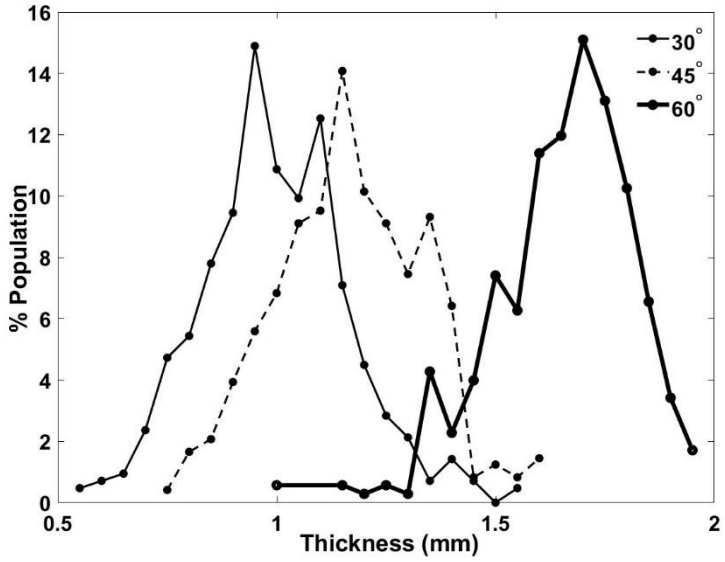

Figure 9 Measured thickness for braided beams with different braid angles

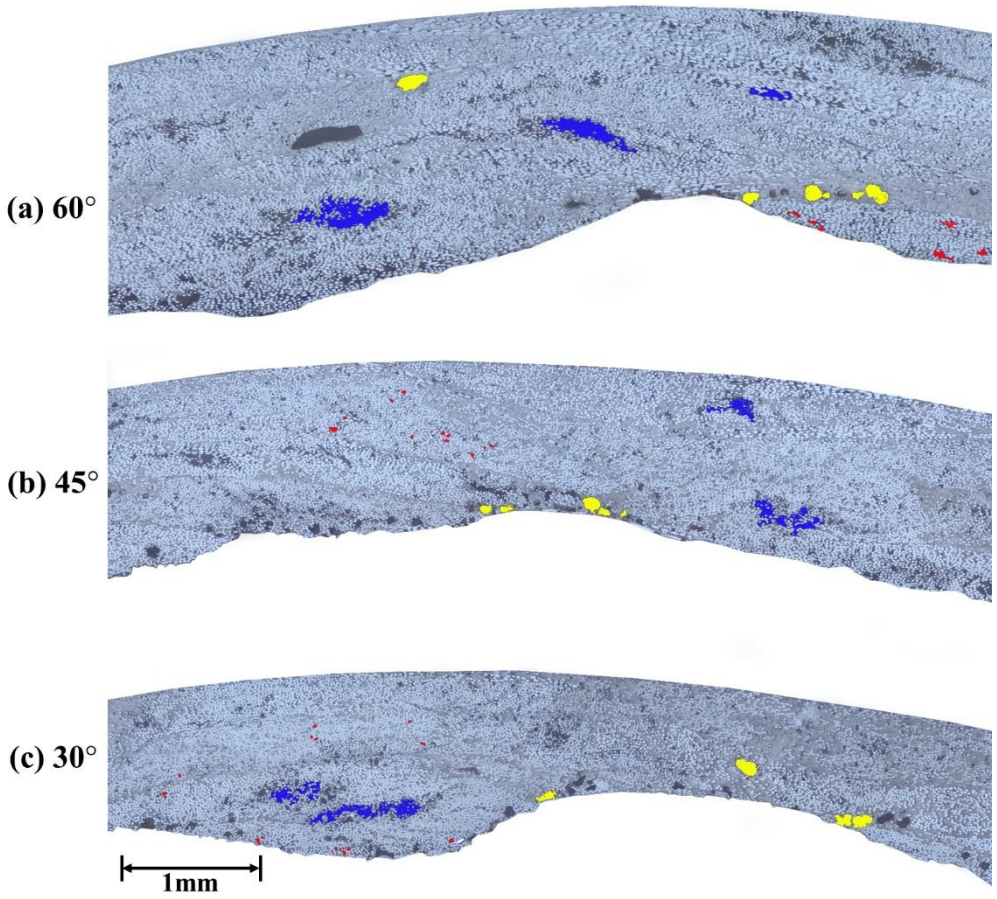

Figure 10 Micrographs of braided beam sections with braid angles of (a) 60°, (b) 45° and (c) 30°. Note: Coloured regions highlight a representative selection (non-exhaustive) of intra-tow micro (Red), intra-tow macro (Blue) and inter-tow voids (Yellow)

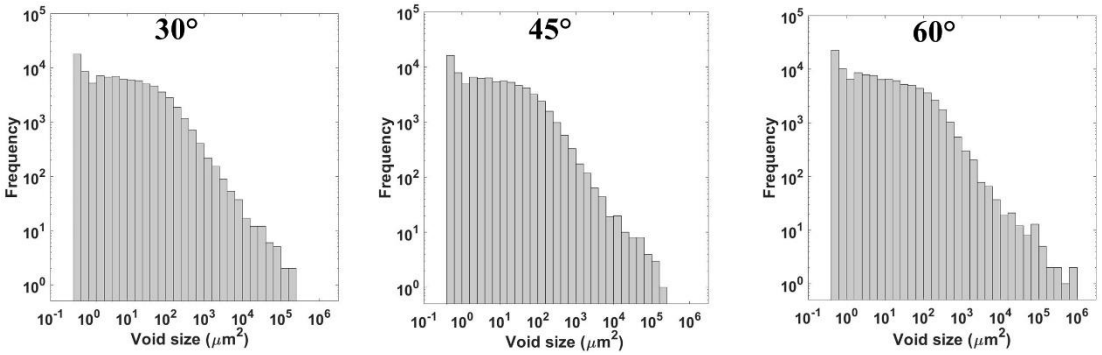

Figure 11 Distribution of void size corresponding to different braid angles

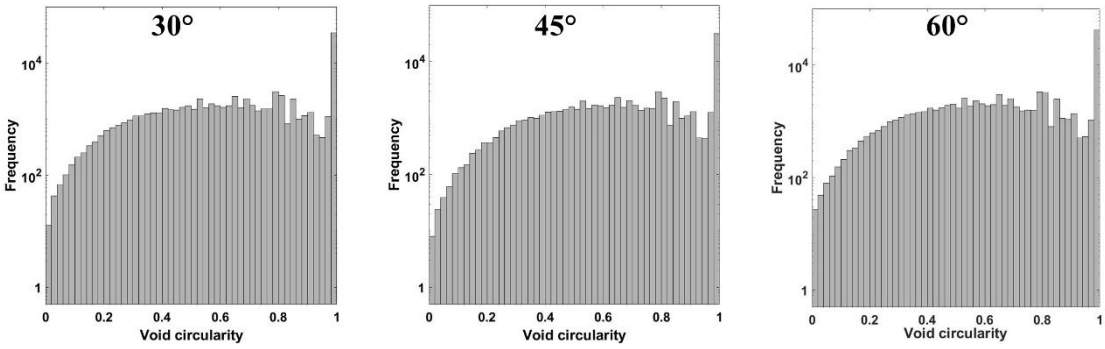

Figure 12 Distribution of void circularity corresponding to different braid angles

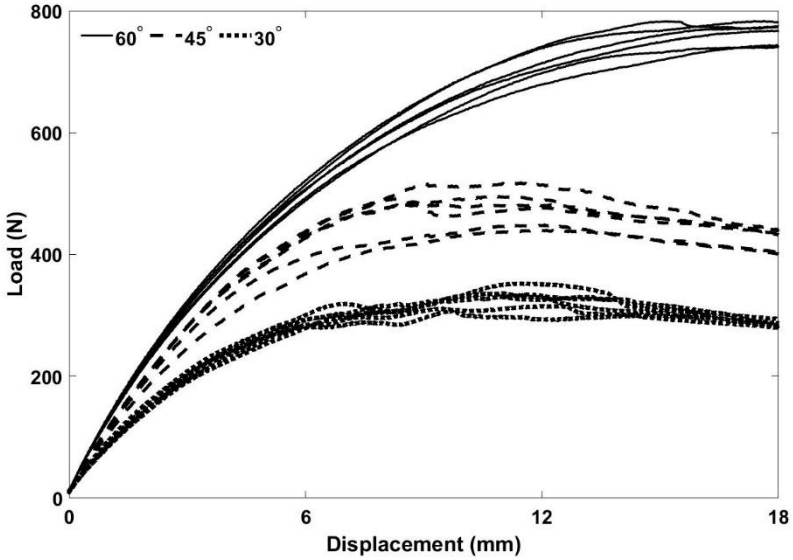

Figure 13 Load-crosshead displacement data from three-point flexure experiments for 6 repeats of each 30°, 45° and 60° beam sets

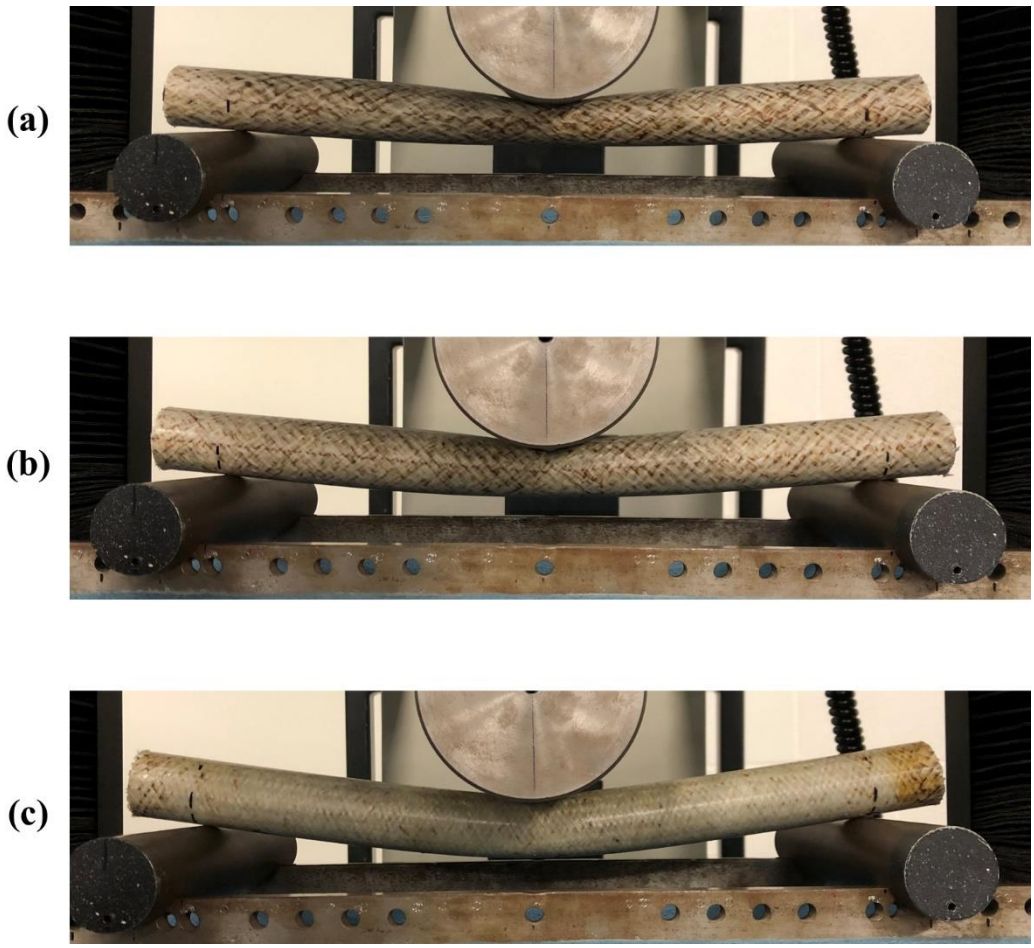

Figure 14 Beams with braid angles of (a) 30°, (b) 45° and (c) 60° in the test fixture after 18 mm of crosshead deflection

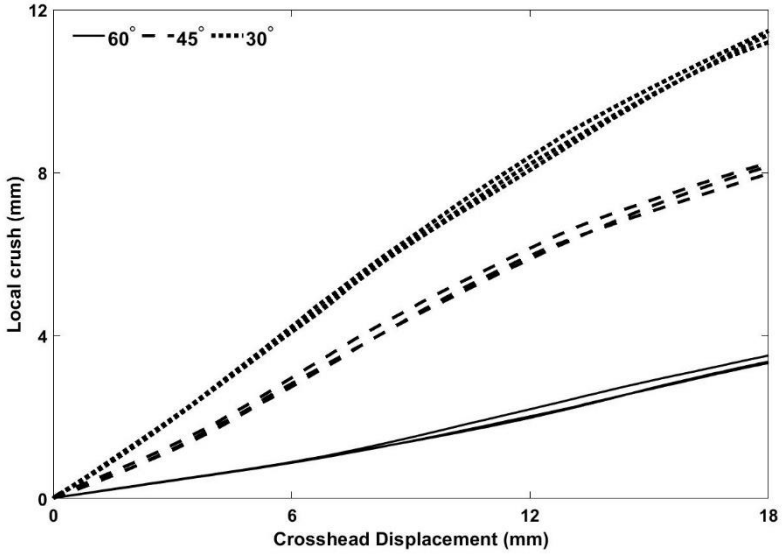

Figure 15 Progression of localised crushing (from the difference between crosshead displacement and the deflectometer displacement) during three-point flexure

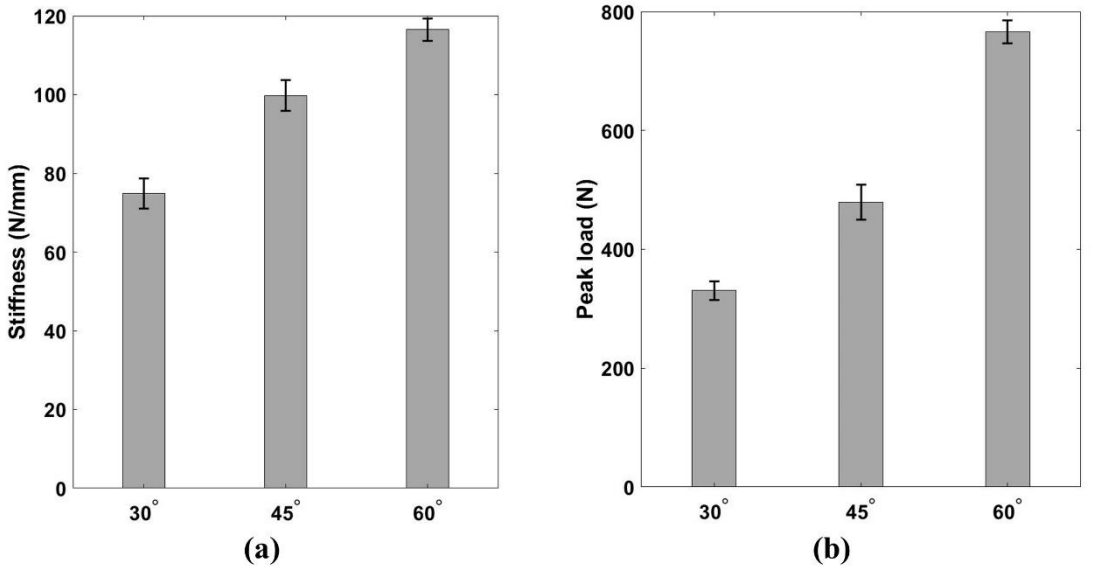

Figure 16 (a) Stiffness and (b) peak load data for different beams. Note: bars represent mean values from 6 repeats and errors represent one standard deviation

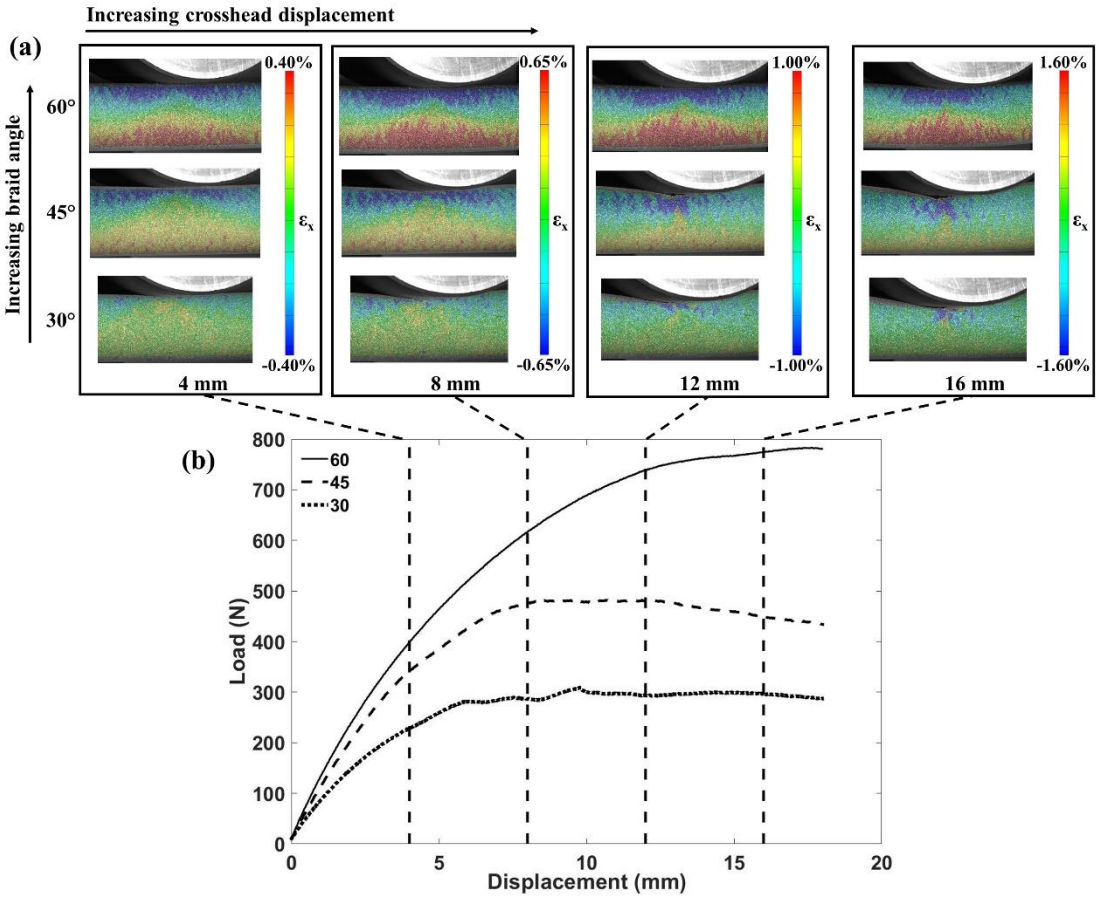

Figure 17 (a) ε_x progression with crosshead displacement during three-point flexure and (b) load-displacement curves corresponding to the beams tested with DIC measurement

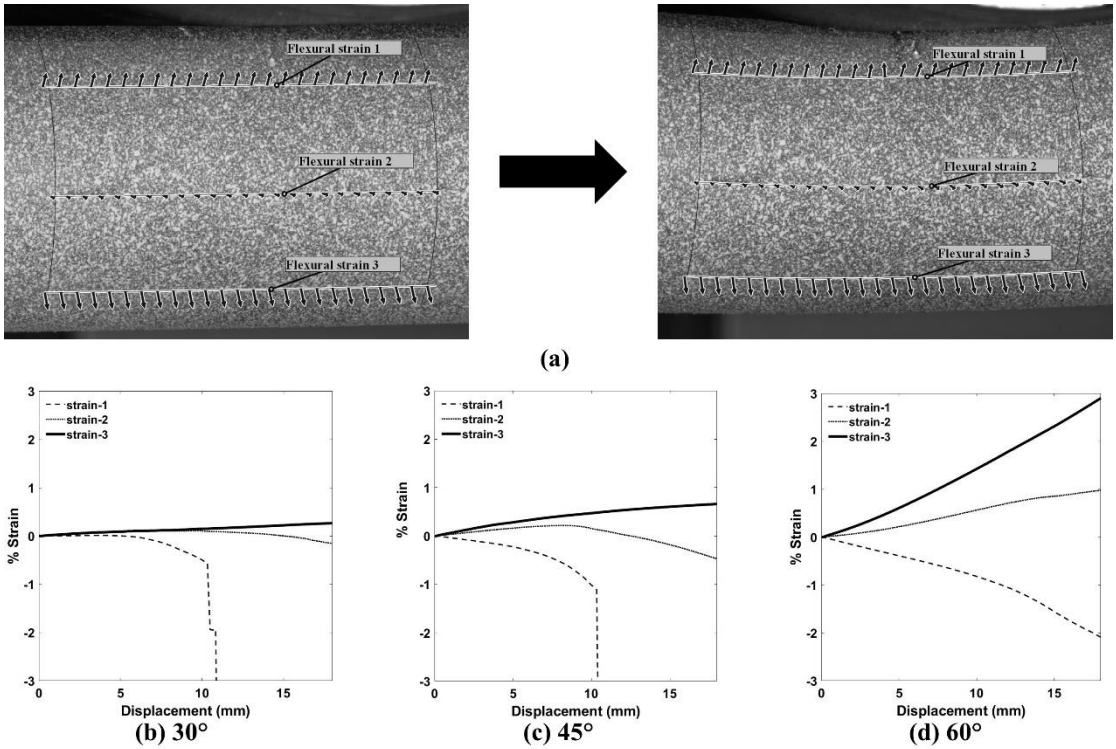

Figure 18 (a) Horizontal sections (strain 1-3) constructed on the surface of a beam showing the initial (preloaded) condition and the condition at increased crosshead displacement. b-d) evolution of flexural strain at 3 locations (strain 1-3) for braided beams during three-point flexure with braid angle of (b) 30°, (c) 45° and (d) 60°

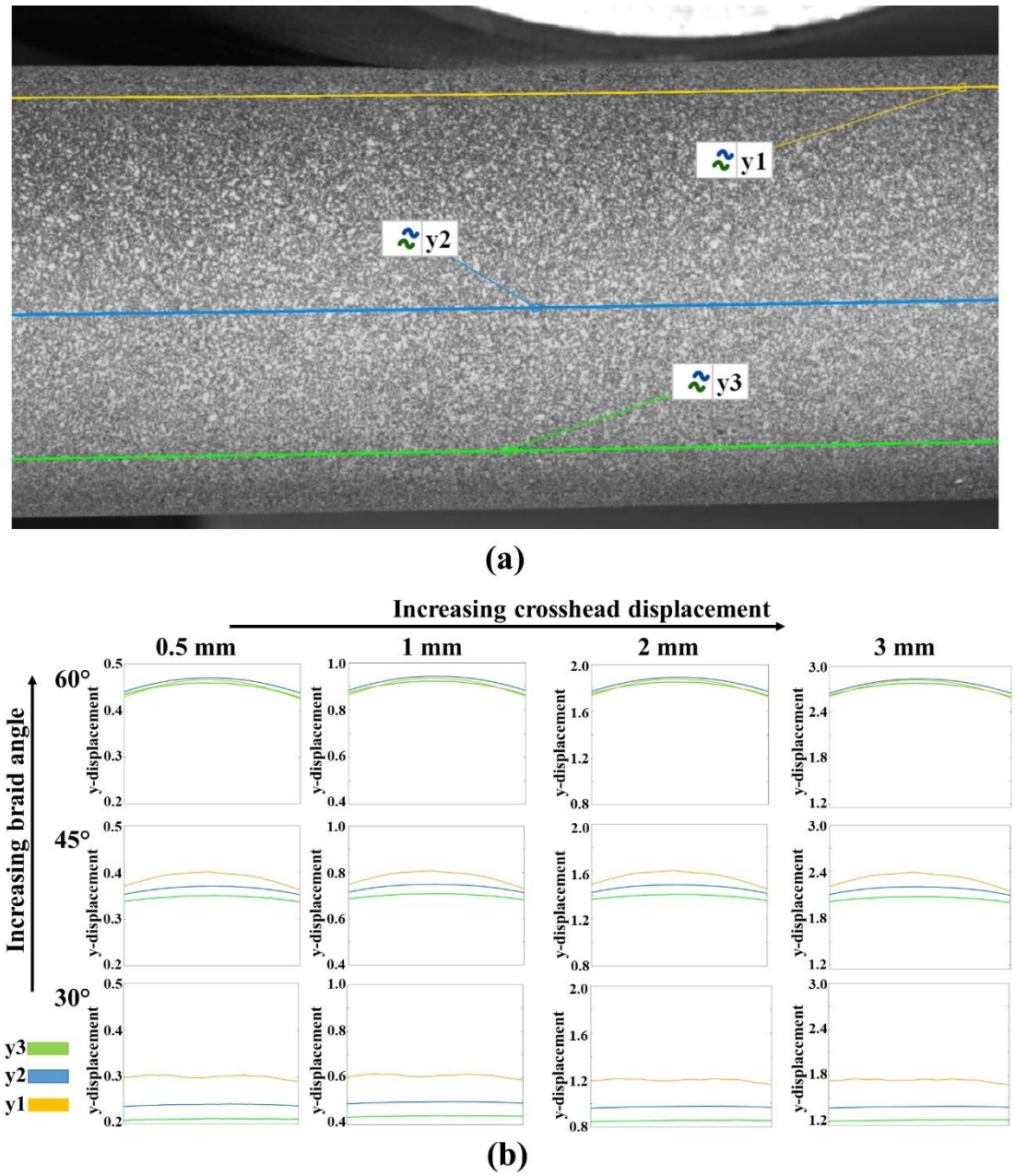

Figure 19 (a) Parallel sections y1-3 for comparing flexural displacements (*y*-, downward in the figure) on the surface of a beam and (b) evolution of downward y-displacement y1, y2 and y3 for beams with different braid angles during three-point flexure (increasing crosshead displacement)

Table 1 Properties of commingled E-glass/PA6 material

Property	Value
Linear weight	1650 g/km
Glass fibre weight fraction	72%
Theoretical fibre volume fraction	54%
E-glass density	2.54 g/ml
PA6 density	1.15 g/ml
PA6 melting point	221 °C
PA6 glass transition temperature	60 °C

Table 2 DIC system parameters employed during acquisition and analysis

Parameter	
Sensor/camera	GOM 12M
Lens	Titanar 100 mm
Image window	4000 pixel × 3000 pixel
Measurement area	150 mm × 100 mm
Calibration plate used	CP20 90 × 72
Facet size	19 pixels (16 pixels step size)
Lens Aperture	f-stop f/16
Depth of field	39 mm
Exposure time	55 to 60 ms (depending on speckle pattern)
Frame rate	2 Hz

Table 3 Mean bias and precision of DIC measurements estimated from static images

Mean bias [ε_x (%)]	Mean precision [ε_x (%)]	Mean bias [dx (mm)]	Mean precision [dx (mm)]	Mean bias [dy (mm)]	Mean precision [dy (mm)]
0.0001	0.0162	0.0029	0.0003	-0.0007	0.0004

Table 4 F_{vf} and V_{vf} estimated from resin burn-off. Note: values represent mean ± std. dev.

	F_{vf}	V_{vf}
30°	48.8 ± 1.1	7.8 ± 1.2
45°	49.9 ± 1.1	8.5 ± 1.2
60°	49.6 ± 1.1	10.5 ± 0.8

Table 5 p-values corresponding to V_{vf} and F_{vf} comparisons obtained from ANOVA

	p-value
V_{vf}	0.002
F_{vf}	0.236

Table 6 q-values obtained from Tukey-Kramer post-hoc analysis performed for V_{vf}. Note: values indicating a statistically significant difference are underlined

Pair	**q (V_{vf})**	**$q_{critical}$**
30°- 45°	1.70	3.67
45°- 60°	4.22	3.67
30°- 60°	5.92	3.67

Table 7 Mean, maximum and minimum thickness values measured for different braided beams. Note: All values are in mm

Thickness	**30°**	**45°**	**60°**
Mean	0.972	1.145	1.630
Maximum	1.503	1.596	1.934
Minimum	0.526	0.747	1.118

Table 8 Tow geometry parameters corresponding to different braided beams. Note: tow width values represent mean ± std. dev.

	30°	**45°**	**60°**
Tow width (mm)	3.18 ± 0.18	2.69 ± 0.16	2.23 ± 0.14
Estimated cover factor	78.3%	80.2%	87.7%

Table 9 p-values corresponding to void size and shape comparison obtained from ANOVA

	p-value
Void size	0.005
Void shape	<0.001

Table 10 q-values obtained from Tukey-Kramer post-hoc analysis performed for void shape and size. Note: values indicating a statistically significant difference are underlined

Pair	**q (void size)**	**q (void shape)**	**$q_{critical}$**
30°- 45°	0.72	15.11	3.31
45°- 60°	4.20	7.97	3.31
30°- 60°	4.80	7.85	3.31